

**Low-energy electron irradiation induced synthesis of molecular nanosheets: An influence of the electron beam energy**

Neumann, C.; Wilhelm, R. A.; Küllmer, M.; Turchanin, A.;

Originally published:

December 2019

**Faraday Discussions 227(2021), 61-79**

DOI: <https://doi.org/10.1039/C9FD00119K>

Perma-Link to Publication Repository of HZDR:

<https://www.hzdr.de/publications/Publ-29910>

Release of the secondary publication  
on the basis of the German Copyright Law § 38 Section 4.



## Low-energy electron irradiation induced synthesis of molecular nanosheets: An influence of the electron beam energy

Journal:	<i>Faraday Discussions</i>
Manuscript ID	Draft
Article Type:	Paper
Date Submitted by the Author:	n/a
Complete List of Authors:	Neumann, Christof; Friedrich Schiller University Jena Wilhelm, Richard; Technische Universität Wien Küllmer, Maria; Friedrich Schiller University Jena Turchanin, Andrey; Friedrich-Schiller-Universität Jena, Institute of Physical Chemistry
<p>Note: The following files were submitted by the author for peer review, but cannot be converted to PDF. You must view these files (e.g. movies) online.</p>	
Neumann etal_ Video S1.mp4	

## ARTICLE

## Low-energy electron irradiation induced synthesis of molecular nanosheets: An influence of the electron beam energy

Christof Neumann,<sup>a</sup> Richard A. Wilhelm,<sup>bc</sup> Maria Küllmer,<sup>a</sup> and Andrey Turchanin<sup>a,d\*</sup>

Received 00th January 20xx,  
Accepted 00th January 20xx

DOI: 10.1039/x0xx00000x

Aromatic self-assembled monolayers (SAMs) can be cross-linked into molecular nanosheets – carbon nanomembranes (CNMs) – via low-energy electron irradiation. Due to their favorable mechanical stability and tunable functional properties, they possess a high potential for various applications including nanosensors, separation membrane for osmosis or energy conversion devices. Despite this potential, the mechanistic details of the electron irradiation induced cross-linking process still need to be understood in more detail. Here we studied the cross-linking of 4'-nitro-1,1'-biphenyl-4-thiol SAM on gold. The SAM samples were irradiated with different electron energies ranging from 2.5 to 100 eV in ultra-high vacuum and subsequently analysed by complementary techniques. We present results obtained via spectroscopy and microscopy characterization by high-resolution X-ray photoelectron spectroscopy (XPS), low-energy electron diffraction with micrometre sized electron beams ( $\mu$ LEED) and low-energy electron microscopy (LEEM). To demonstrate the formation of CNMs, the formed two-dimensional molecular materials were transferred onto grids and oxidized wafer and analyzed by optical, scanning electron (SEM) and atomic force microscopy (AFM). We found a strong energy dependence for the cross section for the cross-linking process, which rates decrease exponentially towards lower electron energies by about four orders of magnitude. We conduct a comparative analysis of the cross sections for the C-H bond scission via electron impact ionization and dissociative electron attachment and find out that these different ionization mechanisms are responsible for the variation of the cross-linking cross section with electron energy.

### Introduction

The interaction of electron beams with matter is widely used in science and technology. Starting with the invention of the first electron microscope by Ernst Ruska<sup>1</sup>, a continuous scientific effort has been undertaken in order to understand and to implement the electron-matter interaction for a variety of applications.<sup>2,3</sup> Nowadays, the imaging of individual atoms with electron beams down to the sub-Ångstrom resolution is possible giving the unprecedented insights into the structure of a variety of materials.<sup>4-6</sup> Furthermore, electron-matter interaction became an important part of the nanotechnology for materials engineering and it is used as a flexible tool for nanofabrication of electronic and photonic devices.<sup>7</sup> Besides the lithographic applications, electron beams can be applied also for materials synthesis (see, *e.g.*, Ref.<sup>8</sup>) and in particular for synthesis of carbon-based nanomaterials such as carbon nanotubes,<sup>9</sup> graphene nanoribbons<sup>10</sup>, onion-like carbon<sup>11,12</sup> or carbon nanomembranes (CNMs).<sup>13</sup> CNMs are an example of organic 2D materials (nanosheets) synthesized by low-energy

electron irradiation of aromatic self-assembled monolayers (SAMs).<sup>14,15</sup> By choice of the molecular compounds for building SAMs, the properties CNMs can flexibly be tuned, *e.g.*, the CNM's thickness<sup>16</sup>, stiffness<sup>17</sup>, chemical functionalization<sup>18</sup> or electric transport.<sup>19</sup> Besides the direct synthesis by electron irradiation, CNMs can be synthesized also by secondary electrons and photoelectrons generated via vacuum UV (VUV) or extreme UV (EUV) irradiation<sup>20</sup> or by secondary electrons generated via helium ions<sup>21</sup>. The electrons predominantly induce cleavage of the C-H bonds in the constituting molecules, which is followed by the creation of new bonds between them and finally the cross-linking of the monolayer.<sup>22</sup> In this way, an aromatic SAM is converted into a 2D molecular material, *i.e.* nanosheet.

Dissociative electron attachment (DEA)<sup>23-25</sup> has been discussed often as a mechanism responsible for the observed cross-linking process.<sup>21,22,26</sup> However, a recent comparative study<sup>27</sup> of the C-H bond scission in [1'',4',1',1]-terphenyl-4-thiol (TPT) SAMs on gold via 6 eV<sup>26</sup> and 50 eV<sup>27</sup> suggest that DEA can prevail only for the cross-linking with 6 eV, whereas for irradiation with 50 eV the electron impact ionisation is dominating. Therewith, the mechanisms of the cross-linking can intimately depend on the electron energy. It has been shown also that the cross-linking leads to reorganisation of the well-ordered pristine SAMs and to the eventual loss of their long-range order.<sup>16,28</sup> Moreover, recent high resolution atomic force microscopy<sup>29</sup> and transmission electron microscopy<sup>30</sup> studies give further insights in the CNM structure and suggest the presence of nanopores

<sup>a</sup> Institute of Physical Chemistry, Friedrich Schiller University Jena, 07743 Jena, Germany

<sup>b</sup> Institute of Applied Physics, TU Wien, 1040 Vienna, Austria

<sup>c</sup> Institute of Ion Beam Physics and Materials Research, Helmholtz-Zentrum Dresden-Rossendorf, 01328 Dresden, Germany

<sup>d</sup> Jena Center for Soft Matter (JCSM), 07743 Jena, Germany

\*Address correspondence to andrey.turchanin@uni-jena.de

Electronic Supplementary Information (ESI) available: [details of any supplementary information available should be included here]. See DOI: 10.1039/x0xx00000x

sized  $\sim 0.5$  nm in these molecular nanosheets. Despite these advances in the understanding of the cross-linking process and the structure of the resulting CNMs,<sup>22, 29-31</sup> the details of their electron irradiation induced synthesis still need to be further elucidated. Thus, the dependence of the cross-linking cross section on the electron energy has not been studied yet in detail, although this knowledge can significantly facilitate understanding of the mechanisms as well as enable a higher level of selectivity and controllability of the electron irradiation induced chemical reactions.

Here we present a detailed study on the cross-linking process of 4'-nitro-1,1'-biphenyl-4-thiol (NBPT) SAMs on gold into CNMs at different electron irradiation energies. We use this particular system, as the conversion of its nitro group into the amino group upon the electron irradiation serves as an indicator for the cross-linking process.<sup>20, 32</sup> This conversion is schematically shown in Fig 1. We irradiated the SAMs using electrons with energies of 2.5, 3.5, 5.0, 6.5, 8.0, 12.6, 50 and 100 eV under ultra-high vacuum (UHV) conditions and studied the conversion using different microscopic and spectroscopic techniques including X-ray photoelectron spectroscopy (XPS), low-energy electron diffraction with micrometre sized electron beams ( $\mu$ LEED) and low-energy electron microscopy (LEEM). In order to evaluate the successful formation of CNMs after irradiation of the NBPT SAMs with different electron energies and doses, these monolayer samples were transferred onto TEM grids and SiO<sub>2</sub> wafers and analysed using optical, scanning electron (SEM) and atomic force microscopy (AFM). We found a strong energy dependence for the cross section for the cross-linking process. The cross-linking rate decreases exponentially about four orders of magnitude towards lower electron energies. We analyse these results by comparing the cross sections for the C-H bond scission via electron impact ionization and dissociative electron attachment and demonstrate that these different mechanisms are responsible for the cross-linking at the high and low electron energy ends of the studied range from 2.5 to 100 eV, respectively.

## Experimental results

First, we characterize by XPS the formation of the NBPT SAM on Au/mica and their cross-linking into CNMs using 50 eV electron irradiation. In Fig. 2A the high-resolution XP spectra for N 1s, S 2p, C 1s and O 1s core level electrons are shown. The N 1s signal of the NBPT SAM consists of a single species at a binding energy (BE) of 405.3 eV (blue) assigned to the nitro group of the NBPT molecule. The sulphur signal has a single doublet due to the formation of thiolates (red) with a BE of the S 2p<sub>3/2</sub> and S 2p<sub>1/2</sub> components at 161.9 and 163.1 eV, respectively.<sup>33</sup> The C 1s signal consist of a main component at a BE of 284.2 eV (red) assigned to the aromatic unit of the NBPT molecule. This peak is accompanied by a shoulder at 285.2 eV due to C-S and C-N bonds (blue). The O 1s spectrum consist of a single species at a BE of 532.4 eV attributed to the nitro group. The effective thickness of the SAM calculated from the attenuation of the Au

4f<sub>7/2</sub> signal is 12 Å. All these spectra confirm the successful preparation of the NBPT SAM according to the literature.<sup>20, 32</sup>

Next, we studied the conversion of the SAMs into CNMs by stepwise irradiation using 50 eV electrons followed by XPS measurements after each step. The respective spectra after the irradiation doses of 5 mC/cm<sup>2</sup>, 15 mC/cm<sup>2</sup>, 20 mC/cm<sup>2</sup>, 40 mC/cm<sup>2</sup> and 50 mC/cm<sup>2</sup> are presented in Fig 2A. In the N 1s spectrum the intensity of the signal of nitro group decreases due to the conversion into the amino group, which arises in the spectra at a BE of 399.3 eV (yellow).<sup>32</sup> A summary of this reduction, presented in Fig 2B, shows that a signal of the amino group can be detected already at electron doses above 2 mC/cm<sup>2</sup> and a complete conversion is found for doses above 20 mC/cm<sup>2</sup>. Note that the total intensity of the N 1s signal decreases to  $86 \pm 5$  % of the initial value for the highest irradiation dose (50 mC/cm<sup>2</sup>) indicating some desorption of nitrogen. In parallel to these changes, also the sulphur spectrum is modified, as seen by the presence of a second S 2p<sub>3/2</sub> species at a BE of 163.3 eV. These species were assigned before to the formation of organosulfides such as R-S-S-R and R-S-R.<sup>22</sup> The fraction of these new species is increasing gradually until their intensity equals to the intensity of the thiolates at an electron dose of 50 mC/cm<sup>2</sup>, Fig 2B. The cross-linking process also modifies the C 1s signal. Due to the formation of new bonds, the full width at half maximum (FWHM) of the peak increases from 1.3 eV to 1.5 eV. Some desorption of carbon can be concluded from a decrease of the C 1s signal to  $92 \pm 3$  % of the initial value. Upon the cross-linking and the conversion of the nitro group, the intensity of the O 1s signal significantly decreases. In agreement with the decrease of the C1s, N1s and O1s intensities; an effective thickness of the monolayer reduces to 11 Å. All these spectral modifications are in good agreement with the previously reported data on the electron irradiation induced changes in NBPT SAMs on gold.<sup>20, 32</sup> Note that according to our previous investigation<sup>22</sup> of a similar molecular system, 1,1'-biphenyl-4-thiols (BPT) SAM on gold, the irradiation with 50 eV electrons at doses up to 100 mC/cm<sup>2</sup> does not lead to further changes in the photoelectron spectra in comparison to the highest dose 50 mC/cm<sup>2</sup> applied in this study.

Next, we studied the cross-linking using low-energy electron microscopy (LEEM). The application of this technique has two advantages. First, the sample is imaged with high surface sensitivity and second, the electron beam is used for imaging as well as for cross-linking a SAM *in operando*. The electron energies used for imaging the NBPT SAM with a sufficient contrast were found to be below 2 eV. Fig S1 A shows a pristine NBPT SAM imaged using an electron landing energy of 1.9 eV. The SAMs were prepared on 300 nm thin polycrystalline Au films thermally evaporated on mica substrates. The grain boundaries of different  $\mu$ m-sized single crystalline Au(111) domains are visible in the LEEM image. The SAM itself appears as a homogeneous bright phase with inclusions of small darker patches. The sample was irradiated continuously with electrons for 90 min and simultaneously imaged. Fig S1 B and C present the same sample region after an irradiation time of 40 min and 90 min, respectively. It can be seen that some darker patches

change the contrast only slightly and do not increase in size. As later shown in this article, the electron dose for cross-linking of a SAM into a CNM for this very low electron energy used for imaging is extremely high. We roughly estimated the applied electron dose during using the field of view, sample current and irradiation time. The resulting value is expected to be below 100 mC/cm<sup>2</sup> and it is orders of magnitude smaller than necessary for cross-linking, as it will be shown later. Note that the dose estimated here has a large uncertainty; nonetheless, we do not assign the small change in contrast between Figs. S1 A, B, and C to the possible cross-linking. The scanning tunnelling microscopy (STM) studies of the densely packed NBPT SAMs on gold have reviewed a polymorphism in in this system with the phases exhibiting different unit cells and therefore different packing density.<sup>34</sup> We attribute the variation of the LEEM contrast to these different phases in the NBPT SAM and their possible reorientation during the imaging. As discussed later, we can exclude also the variation of contrast due to a possible carbon deposition upon the LEEM imaging.

In order to study the cross-linking process by LEEM in more detail we used an irradiation energy of 50 eV. We have found that the direct imaging of the SAMs using this beam energy does not reveal any contrast in the images. Therefore, we irradiated the sample stepwise for 3 s with 50 eV beam energy and afterwards imaged the sample using a beam energy of 1.5 eV. The resulting image series is presented in Fig 3 A – G. Already after an irradiation time of 3 seconds a clear contrast change is visible. A fraction of the darker patches is significantly increased. We assign this change to the growing CNM domains. By further increasing the irradiation time, the contrast of the LEEM image shows merging of the CNM patches (see Fig 3 E). This trend continues until in Fig 3 G the image contrast becomes almost uniform and the dark area covers ~90 % of the total field of view indicating a conversion of the SAM into a continuous nanosheet. A similar topography of the conversion a NBPT SAM on gold into a CNM was also reported earlier by helium ion microscopy (HIM) as a function of the He<sup>+</sup> irradiation dose using the primary He<sup>+</sup> energy of about 37 keV.<sup>21</sup> The clear contrast between the CNM and the non-irradiated SAM region is even more visible in a larger field of view after obtaining the image series, Fig. 3 A-G. The cross-linked region appeared as a dark circle, Fig 3H. To estimate the applied electron dose in the image series presented in Fig. 3, we employed the same procedure as described in the previous paragraph and found it of a comparable value as applied for the complete nitro-to-amino conversion with the same electron beam energy (50 eV) in Fig 2.

As mentioned above, the deposition of carbon by the electron beam may also lead to this contrast change. Note, that excellent vacuum conditions of  $\sim 1 \times 10^{-10}$  mbar are required for performing LEEM making a strong carbon deposition unlikely. Nevertheless, we investigated a bare Au/mica sample using comparable imaging parameters as a reference. The LEEM image in Fig S2A shows the Au/mica surface with different domains divided by bright domain boundaries. In the central region of the image, a slightly brighter circle indicates the region

illuminated by the electron beam before. As no SAM was grown on this sample, the change in contrast can be exclusively assigned to carbon deposition. Nevertheless, the contrast change in the LEEM images, due to the cross-linking, is much stronger in comparison to the carbon deposition (see Fig 3H). Furthermore, the circular region in Fig S2A is brighter in comparison to the non-illuminated area, which is different to Fig. 3H, clearly demonstrating that the dark patches observed in Fig 3 are due to the cross-linked regions.

Next, we performed low-energy electron diffraction with  $\mu$ m-sized electron beams ( $\mu$ LEED) to study the cross-linking process. As known from previous reports, aromatic SAMs including the precursor molecule NBPT form highly ordered structures on Au(111) surfaces.<sup>16, 31, 34</sup> First, we analysed bare Au/mica substrate after its pre-annealing (see Experimental for details) showing a pattern at a beam energy of 42.7 eV (Fig S2B). This pattern consists of the signatures of several Au(111) domains oriented at different angles within the beam spot size of  $\sim 15$   $\mu$ m (see Experimental for details). The pattern was obtained close to the bright domain boundaries, which are most likely clean Au areas. After growth of the NBPT SAM, the  $\mu$ LEED pattern due to Au (111) at 42.7 eV vanishes because of a high surface sensitivity of LEED only showing diffraction on the topmost layer. As the thiols strongly interact with the gold atoms forming covalent bonds,<sup>35, 36</sup> the formation of densely packed NBPT SAM reconstructs the topmost gold layer.<sup>34</sup> Therefore, the peaks with the hexagonal symmetry due to Au(111) plane can be found only at higher beam energies like 204 eV and 313 eV (see Fig S2 C and D), which access deeper layers in the gold substrate. Instead of the substrate signal at 42.7 eV a new pattern due to the NBPT SAM arises at a beam energy of 12.6 eV, Fig 4A. The observed diffraction pattern suggests the SAM molecules form a  $(9 \times 3\sqrt{3})R10^\circ$  unit cell on Au(111) (Fig 4B and C). This result is in a good agreement with the previous STM and LEED results.<sup>34</sup> The same unit cell, however, with  $R0^\circ$  was assigned<sup>34</sup> to the  $\gamma$ -phase with a surface area per molecule of 48.5  $\text{\AA}^2$ . As mentioned above, the STM study revealed a polymorphism in this SAM; the  $\alpha$ -phase, having a higher packing density (27.4  $\text{\AA}^2$ /per molecule), was found to dominate the surface at a full coverage.<sup>34</sup> In our study, we only observed the  $\gamma$ -phase by  $\mu$ LEED, however, referring to the STM data, we assume a coexistence of different phases on the surface of our samples.

The electron irradiation induced cross-linking of the aromatic NBPT SAMs into CNMs modifies their structure by creation of new intermolecular bonds. This leads to the loss of the long-range order in the sample and therefore to the vanishing of the  $\mu$ LEED pattern.<sup>16, 28</sup> We performed the  $\mu$ LEED analysis in the same LEEM instrument, which enabled us to monitor this transition *in operando*. In contrast to the previously obtained  $\mu$ LEEM data we could use here an accurate calibration of the incoming electron flux for a quantitative analysis (see Experimental for details). Video S1 presents the evolution of the  $\mu$ LEED pattern with an increasing electron dose. The intensity of the pattern decreases constantly until no pattern is visible for doses above 17 mC/cm<sup>2</sup>. Fig 4D presents the normalised intensities of the zeroth, first and second diffraction order

analysed [Video S1](#). The intensities of the higher diffraction orders decrease faster with non-permanent velocities while the zeroth order vanishes slower with a nearly constant velocity. This is another confirmation that the electron beam firstly leads to creation of new bonds between the molecules lifting the previously ordered structure. This effect is followed then by the reconstruction of the gold surface and changing the roughness of the sample which finally leads to vanishing of the zeroth order spot. A similar behaviour was observed also for 1,1'-biphenyl-4-thiols (BPT) SAMs on Cu(111) by STM and LEED after the respective electron irradiation steps.<sup>28</sup>

Next, we analyse the influence of the electron energy on the cross-linking. We employed a variety of different electron energies between 2.5 – 100 eV to this end. To correlate these results with the LEEM and  $\mu$ LEED data, we included electron energies of 12.6 eV and 50 eV in our study. The cross-linking process was tracked *in situ* using XPS after stepwise electron irradiation in the same UHV chamber. We used the N 1s XP signal, i.e. the nitro-to-amino conversion, as an indicator for the cross-linking (c.f. [Fig 2A](#)).

A summary of the nitro-to-amino conversion for all electron energies applied for the cross-linking is presented in [Fig 5](#). These results show that the cross-linking process of a CNMs significantly depends on the energy of impinging electrons. At an electron energy of 100 eV, it is most efficient within the studied electron energy range. Thus, already after an irradiation dose of 15 mC/cm<sup>2</sup> only amino groups are detected by XPS. Using this observation as an indicator of the cross-linking, it is seen from [Fig. 5A](#) for a beam energy of 12.6 eV the cross-linking rate is significantly reduced in comparison to 100 eV. A comparison of the XPS results with the  $\mu$ LEED data in [Fig 4](#) provides a correlation to the respective structural changes. For electron doses <17 mC/cm<sup>2</sup> the cross-linking leads to vanishing of the  $\mu$ LEED pattern, however, the nitro-to-amino conversion is not yet complete, it is only ~40 % of this particular electron dose. For a full nitro-to-amino conversion, an electron dose is required which is ~9 times higher (150 mC/cm<sup>2</sup>). These observations illustrate that already a partial cross-linking is sufficient to lift the long-range order in the NBPT SAM, however, a complete cross-linking is achieved at much higher electron doses.

By lowering further the electron energy, the cross-linking rate decreases dramatically. As seen from [Fig 5](#), the electron dose using the energies of 8, 6.5, 5, 3.5 and 2.5 eV increases by orders of magnitudes. Especially the cross-linking with an electron energy of 2.5 eV requires ~65000 mC/cm<sup>2</sup> making the CNM synthesis at these energies to a very inefficient process.

Finally, to prove the successful synthesis of CNMs, we transferred the irradiated monolayers onto SiO<sub>2</sub>/Si wafers and transmission electron microscope (TEM) grids (see Experimental for details) and analysed the samples by optical, scanning electron and atomic force microscopy. [Fig. 6](#) presents an overview of transferred samples irradiated with an electron energy of 12.6 eV at different electron doses. The samples were chosen at nitro-to-amino conversion ratios of 40 % (17

mC/cm<sup>2</sup>), 60 % (50 mC/cm<sup>2</sup>), 80 % (100 mC/cm<sup>2</sup>) and 100 % (150 mC/cm<sup>2</sup>). [Fig 6A](#) presents a SEM image of a NBPT SAM irradiated with 17 mC/cm<sup>2</sup> after transfer on a TEM grid showing no freestanding membrane. As seen by from the  $\mu$ LEED results ([Fig. 4D](#)), this electron dose leads to cross-linking of a sufficient amount of molecules to eliminate the long-range order in the sample, however, the fabrication of a freestanding continuous CNM is not yet achieved. Nevertheless, a transfer of CNM patches onto a SiO<sub>2</sub>/Si wafer was already possible, as seen by an optical microscope image of a sample irradiated with the same electron dose, [Fig. S3](#). This result demonstrates that the nitro-to-amino conversion of 40 % is already sufficient for the formation of CNM patches but a continuous CNM is not yet formed. The SEM and AFM images in [Fig. 6E and I](#) confirm this conclusion. Thus, by AFM we observe the surface roughness root mean square (RMS) > 1 nm for the samples irradiated with 17 mC/cm<sup>2</sup> and transferred onto SiO<sub>2</sub> substrates with the intrinsic RMS roughness below 0.2 nm. For higher irradiation doses, freestanding CNM fragments became visible in the SEM images. The prolonged irradiation leads to sufficiently large cross-linked fragments which cover the edges (50 mC/cm<sup>2</sup>) or almost the complete holes (100 mC/cm<sup>2</sup>) of the TEM grids as seen from [Figs. 6B and 6C](#), respectively. The patch-like structure in the CNM is still recognized, as seen by the SEM ([Fig. 6F and G](#)) and AFM ([Fig. 6J and K](#)) analysis, after the transfer on SiO<sub>2</sub>. The RMS roughness is 0.6 ± 0.1 nm for samples irradiated with 100 mC/cm<sup>2</sup> confirming the merging of the CNM patches towards a continuous film. This trend is further observed after an applied electron dose of 150 mC/cm<sup>2</sup>. The SEM image in [Fig. 6D](#) shows a continuous CNM without macroscopic defects covering holes of the TEM grid. Note that the rupture on the left-hand side is shown to introduce a better contrast in the image otherwise the CNM was continuous. Additionally, the SEM and AFM images in [Fig. 6H and L](#) confirm a completed structural change of the NBPT SAM into a CNM. The transferred molecular nanosheet reveals a smooth topography with a RMS roughness of 0.3 ± 0.1 nm. These microscopy results confirm that the employed nitro-to-amino conversion rate can be used as a suitable measure for the cross-linking of a NBPT SAM into a CNM.

## Discussion

The experimental results presented above demonstrate a strong dependence of the electron dose required for complete cross-linking of a NBPT SAM on gold into a CNM on the applied electron energy, [Fig. 5](#). The dose increases approximately by four orders of magnitude by decreasing the electron energy from 100 to 2.5 eV. Based on these data, we obtain the respective effective cross sections of the cross-linking and the cross-linking rates as a function of the electron energy.

We analyse the cross-linking rates based on a formal description of the conversion of an aromatic SAM into a CNM via the following chemical reaction:



where [SAM] and [CNM] represent the fractions of nitro groups and amino groups in a monolayer, respectively. The reaction rate can be represented then as:

$$\frac{d[\text{SAM}]}{d\phi} = -\kappa[\text{SAM}], \quad \text{Eq. 2}$$

where  $\kappa$  is the rate constant with units  $\text{mC}/\text{cm}^2$ . Therewith, we derive the following kinetic equation (see SI for details):

$$F(\Phi) = [\text{CNM}](\Phi) = 1 - e^{-\kappa\Phi}, \quad \text{Eq. 3}$$

which describes the conversion rate of a NBPT SAM into a CNM as a function of the electron irradiation dose. We apply Eq. 3 to fit the experimental data presented in Fig 5A and the statistical analysis demonstrates that with Eq. 3 the conversion rates can be described very well for all studied electron energies (see Fig. S4 A-D and Table S1). The obtained rate constants are presented in Fig. 7A and in Table S2. It has been suggested<sup>27, 37</sup> that these values, if recalculated in unites [number of electrons]/ $\text{cm}^2$  can be employed as a measure for the effective cross sections,  $\sigma_{\text{eff}}$ , representing the electron irradiation induced modifications of a SAM. Note that therewith the obtained  $\sigma_{\text{eff}}$  values, see Fig. 7A and Table S2, represent some integral quantities accounting for various processes occurring in a NBPT SAM upon its conversion into a CNM such as (i) scission of the C-H bonds; (ii) formation multiple bonds between the molecules; (iii) possible opening of the aromatic rings; (iv) chemical and structural changes at the sulphur/gold interface; (v) reorientation of the molecules and molecular fragments in the monolayer upon the cross-linking; (vi) the nitro-to-amino reduction, (vii) energy distribution of the secondary electrons; (viii) possible radical reaction<sup>26</sup>; etc.

As seen from Fig. 7A, the  $\sigma_{\text{eff}}$  value for 50 eV obtained in this study is in a good agreement with the respective value measured in a similar molecular system [1'',4',1',1]-terphenyl-4-thiol (TPT) SAM on gold via analysis of the C-H bond scission employing high resolution electron energy loss spectroscopy.<sup>27</sup> As was analysed in Ref.<sup>27</sup>, for irradiation with this electron energy the prevailing mechanism of the C-H bond scission and the cross-linking is due to the direct electron impact ionization. The cross sections of the dissociative electron attachment (DEA) or of the electronic excitations, which can also lead to the C-H bond scission and cross-linking, are three orders and one order of magnitude smaller, respectively, than the cross section of the electron impact ionization.<sup>27</sup> Indeed, in Ref.<sup>26</sup> the DEA resonance leading to the C-H bond scission of in a TPT SAM was found to be at 6 eV with a width of  $\sim 3$  eV. The effective cross section of the chemical modification of a TPT SAM per molecule was estimated to  $1.2 \times 10^{-16} \text{ cm}^2$  at irradiation with 6 eV electrons.<sup>27</sup> Taking into account a fraction of the secondary electrons generated by the gold substrate with an energy of the DEA resonance, the DEA cross section for 50 eV was estimated to be  $3-8 \times 10^{-18} \text{ cm}^2$ ,<sup>27</sup> which significantly smaller than the cross section value of  $1.4 \times 10^{-15} \text{ cm}^2$  for the direct electron impact ionization of such a related aromatic hydrocarbon as benzene.<sup>38, 39</sup>

A comparison of the calculated cross section for the direct electron impact ionization of benzene<sup>38, 39</sup> with the experimentally measured cross-linking cross sections for the

NBPT SAM at 12.6 and 100 eV shows an excellent qualitative agreement. The respective cross sections decreases in both cases by a factor of  $\sim 12$  towards low electron energies. However, the absolute values for the direct electron impact ionization cross sections of  $1.2 \times 10^{-16} \text{ cm}^2$  and  $1.5 \times 10^{-15} \text{ cm}^2$  for the electron energies 12.6 eV and 100 eV, respectively, differ by two orders of magnitude from the effective cross-linking cross sections. We attribute this difference to various processes besides the C-H bond scission listed as (ii) – (viii) (see above) occurring in the NBPT SAM upon its conversion in to a CNM. Based on these results we conclude that in the studied energy range 12.5 – 100 eV, the cross-linking via direct electron impact ionization is the prevailing mechanism for the C-H bond scission resulting in the formation of a CNM. This conclusion is further supported by an analysis of the cross-linking rate constants in the whole studied electron energy range, Fig. 7.

As seen from Fig. 7B, the electron energy dependence of the rate constants follows well an Arrhenius-type equation

$$\kappa = \kappa_0 e^{-\frac{\epsilon}{E}}, \quad \text{Eq. 4}$$

where  $E$  is energy of the impinging electrons,  $\kappa_0$  is a pre-exponential factor and  $\epsilon$  is a quantity analogous to the activation energy in a thermally excited chemical reaction. Fig. 7B shows that by the linearization of Eq. 2 two electron energy regions 2.5 – 6.5 eV and 6.5 – 100 eV with the respective  $\epsilon$  values of  $\epsilon_1 = 13.2 \pm 1.8 \text{ eV}$  and  $\epsilon_2 = 37.5 \pm 2.1 \text{ eV}$  can be identified. It is peculiar that the energy of 6.5 eV matches well to the above mentioned DEA resonant processes in the TPT SAM at  $\sim 6 \text{ eV}$ .<sup>27</sup> We relate this change in the slope to different mechanisms of the C-H bond scission resulting in the cross-linking at low and high electron energies studied in our work. Whereas for high electron energies the direct electron impact ionization can be identified as the prevailing mechanism for the cross-linking, already at 10 eV its cross section takes a value of  $2.1 \times 10^{-17} \text{ cm}^2$ , which as an order of magnitude smaller than the DEA cross-section for the TPT SAMs at 6 eV irradiation.<sup>26</sup> The observed change in the slope in Fig. 7B corresponds well to this DEA resonance energy observed in the chemically akin aromatic NBPT SAM.

Note that for a more accurate determination of the  $\sigma_{\text{eff}}$  values not only primary electrons but also the secondary electrons generated by the gold substrate have to be taken into account. Moreover, one has to consider also the spectral distribution of the secondary electrons for a certain energy of the primary electrons. As has been shown in Ref.<sup>40</sup> for a clean gold substrate and for a 1-hexadecanethiol SAMs on gold, depending on the electron energy in the range from 5 to 100 eV, the secondary electron spectrum is either dominated by elastically scattered electrons (low energies) or by true secondary electrons (high energies) with a maximum intensity  $\sim 3 \text{ eV}$ . For primary electron energies below a value of the work function of gold ( $\sim 5.3 \text{ eV}$ ), the secondary electron peak consists only of the elastically scattered primary electrons and has the secondary electron yield (SEY) of 1.<sup>41</sup> Taking into account these contributions as well as the experimental values of the SEY on gold with the carbonaceous layers<sup>40, 41</sup>, and considering different relevant

cross sections discussed in the previous paragraph, we estimated the respective SEY contributions to the irradiation process (see Table S3 details). With these values, the corrected effective cross sections  $\sigma_{\text{eff}}^*$  were calculated, which are presented in Fig. 7B and Table S2. In general, the  $\sigma_{\text{eff}}^*$  values, due to the SEYs, are smaller than the  $\sigma_{\text{eff}}$  values, this difference increases towards lower electron energies as the relevant SEY increases from 0.2 for 100 eV to 1 for primary electron energies of 5 eV and lower energies.

The effective cross section values of the cross-linking of a NBPT SAMs into a CNM could be defined even more accurately, if the precise surface density of the NBPT molecules on Au(111) would be known for the studied samples. However, due to the observed polymorphism in this SAM,<sup>34</sup> discussed in the results section, this information was not available in our study. Taking into account that in the densely packed NBPT SAM a mixture of the  $\alpha$  and  $\gamma$  phases with the respective surface areas per molecule of 27.4 Å<sup>2</sup> and 48.5 Å<sup>2</sup>, is possible<sup>34</sup>, one could expect ~50 % uncertainty of the  $\sigma_{\text{eff}}^*$  values presented in Table S2.

Finally, the C-H bond scission driven by different mechanisms at for low and high electron energies, Fig. 7, may result in the cross-linking of NBPT SAMs into CNMs with varying structure depending on the employed electron energy. We conducted a detailed comparative analysis of the XPS data in Fig. 2 for cross-linking at 50 eV electrons with the respective data for cross-linking at 5 eV electrons, see Fig. S5. We could not find any significant difference between both data sets with an exception of a reduced carbon loss for the sample cross-linked at 5 eV, which was ~3 % lower in comparison to the sample cross-linked at 50 eV. Here a further structure sensitive investigation is necessary to elucidate this difference and to find out the microscopic differences between CNMs cross-linked via these different C-H scission mechanisms.

## Summary and Conclusions

We experimentally studied the electron irradiation induced modification of NBPT SAMs on gold using electron energies in the range of 2.5 - 100 eV. We found that for all applied energies the SAMs can be cross-linked into molecular nanosheets – carbon nanomembranes (CNMs). Our low-energy electron diffraction and microscopy data demonstrate that upon the irradiation the long-range order of a pristine NBPT SAM is lifted due to the cross-linking. At the initial stages, CNM patches form in the monolayer and they grow and merge into a continuous molecular nanosheet with the proceeding electron irradiation. A detailed X-ray photoelectron spectroscopy study enabled us to determine the electron energy dependent cross-linking rates and the respective effective cross sections of the cross-linking. The cross-linking rate and the effective cross section at the lowest studied electron energy (2.5 eV) are smaller by about four orders of magnitude in comparison to the highest studied electron energy (100 eV). Our analysis of the cross-linking rates for various electron irradiation energies enabled us to obtain the energy dependent effective cross sections of the cross-linking. By comparing these cross section values with the cross-

sections of different electron beam induced ionization processes in aromatic hydrocarbons it was possible to identify two different mechanism of the C-H bond scission leading to the cross-linking at high and low electron energies. At the high electron energies, the cross-linking is dominated by the direct electron impact ionization, whereas at the low electron energies, close to 6 eV, the dissociative electron attachment prevails. In accord with a presence of these two mechanisms, the electron energy dependent cross-linking rates can be described well by an Arrhenius-type equation with two different exponents for ranges of 2.5 – 6.5 eV and 6.5 – 100 eV. We expect that the obtained results will further facilitate the tailored synthesis of two-dimensional materials and in particular molecular based two-dimensional materials with engineered functional properties via the electron irradiation induced chemical reactions.

## Experimental

### Preparation of self-assembled monolayers (SAMs)

Self-assembled monolayers (SAMs) of 4'-nitro-1,1'-biphenyl-4-thiol (NBPT; Taros 99%; sublimated before use), were formed on 300 nm thermally evaporated Au on mica substrates (Georg Albert PVD-Coatings). First the substrates were cleaned in an O<sub>2</sub> plasma-cleaner (Diener electronics), rinsed with ethanol (VWR, HPLC grade) and blown dry in a stream of nitrogen. They were then immersed in a ~0.1 mmol solution of NBPT in dry, degassed *N,N*-dimethylformamide (DMF, Alfa Aesar 99.9%) for 72h in the dark in a sealed flask under nitrogen. Afterwards samples were rinsed with DMF (VWR, HPLC grade) and ethanol and blown dry with nitrogen.<sup>20, 32</sup> The SAMs were stored under inert atmosphere or directly used after preparation.

### Cross-linking of NBPT SAMs into carbon nanomembranes (CNMs)

Electron irradiation was performed in the same UHV system used for the XPS analysis. The UHV chamber used for cross-linking with low energy electrons is constructed from  $\mu$ -metal for shielding of external electromagnetic fields. The electron irradiation was conducted by a NEK-150-SC (Staib) electron gun using energies in the range of 8 – 100 eV, which are generated with an absolute accuracy of 0.25 eV. To access electron energies of 2.5 – 8 eV a negative sample bias voltage was applied (see below). To gain a homogeneous irradiation of the SAM, the electron beam is scanned using the scanning unit of the NEK-150-SC and calibrated using a faraday cup placed on the manipulator. The cross-linking was performed at a pressure  $< 1 \times 10^{-9}$  mbar. As at primary electron energies of 2.5 – 6.5 eV the electron flux of the electron gun decreases significantly, to overcome this drawback, we used a primary electron energy of 12.6 eV and decelerated the electrons with a negative retarding voltage in front of the sample to achieve the desired low electron energies for irradiation. In Fig S5a comparison the nitro-to-amino conversion of a sample irradiated with 8 eV and a sample irradiated with 12.6 eV primary electron energy slowed down to 8 eV is shown. The data coincide well and enable us to exclude possible artefacts; therewith we used

negative retarding voltages to decelerate 12.6 eV primary electrons to 2.5, 3.5, 5 and 6.5 eV.

#### Transfer of CNMs

In order to transfer the CNMs onto SiO<sub>2</sub>/Si wafers (Sil'Tronix with 300 nm of dry thermal oxide) and onto TEM grids (Quantifoil R 2/2 on Cu 400 mesh) we used the following procedure. Firstly, a poly(methyl methacrylate) layer (PMMA, AR-P 631.04, Allresist GmbH) was spin-cast onto the surface for 40 s at 2000 rpm and the CNM/PMMA sandwich was heated on a hotplate at 90 °C for 5 min. Afterwards, a second PMMA (AR-P 671.04, Allresist GmbH) layer was spin-cast and baked. The gold layer was separated from mica as described in the literature.<sup>42</sup> Next, the gold was etched in a potassium iodine solution (I<sub>2</sub>/KI/H<sub>2</sub>O in mass proportion of 1:4:10) for 10 min. After cleaning by floating on surface of aqueous Na<sub>2</sub>SO<sub>3</sub> solution (Carl Roth, 74 mmol/l) and ultrapure water for 5 minutes, the PMMA/CNM sandwich was then transferred onto the new target substrate, dried with a gentle flow of nitrogen and annealed on a hot plate at 90 °C for 15 min. PMMA was removed by immersion in acetone (VWR, HPLC grade) for 1 h. The CNM on SiO<sub>2</sub>/Si substrate were afterwards rinsed in isopropanol (VWR, HPLC grade) and blown dry with a stream of nitrogen. CNMs on TEM grids were treated in a critical point dryer (Tousimis Autosamdri-815) to minimize damage on freestanding parts.<sup>43</sup>

#### Optical microscopy

The optical microscope image was obtained using a Zeiss Axio Imager Z1.m microscope equipped with a 5 megapixel CCD camera (AxioCam ICc5) in bright field operation.

#### Low energy electron microscopy and low energy electron diffraction

LEEM and  $\mu$ LEED were performed with an Elmitec LEEM-III system equipped with a field-emitted cathode (FEC) and an energy analyser. For imaging start voltages (StV), i.e. electron landing energies, between 0 and 2 eV were used. The use of a contrast aperture is indicated in the respective images. LEED was performed with an illumination aperture leading to LEED pattern from an area of about 15  $\mu$ m in diameter ( $\mu$ LEED). The Au/mica sample was prepared for the measurement using several annealing steps. First 200 °C for 12h, followed by 300 °C for 2h and finally 330 °C for 12h. The NBPT SAMs were only heated to 80 °C for 12 h in order to prevent thermally induced desorption of the molecules. Note that standard preparation procedures such as sputter cleaning and high temperature annealing cannot be applied for these samples. LEED pattern were found only for a narrow range of StVs for samples covered with SAMs (10-17 eV) in addition to peaks with hexagonal symmetry at 204 eV, 313 eV, 352 eV, and 392 eV associated with pattern from the Au(111) substrate. For a Au(111) sample without SAM the contrast at 10-17 eV is absent and additional patterns at 42.7 eV, 58.9 eV, 93.1 eV were observed. To calibrate the incoming electron flux in LEEM/LEED for quantitative determination of the fluence dependence of the LEED contrast, the emission from the FEC was adjusted and kept constant and an illumination aperture was used. The latter

determines together with the adjusted magnification the exposure area at the sample. Subsequently, the sample was biased to negative voltage (negative StV), such that all incoming electrons are reflected in front of the surface (no inelastic losses in the sample) into the detector column. No contrast aperture is used and the optics are adjusted to LEED-mode. The bias voltage at the multi-channel plate (MCP) detector was switched off and the incoming current of electrons on the front side of the MCP was directly measured. Together with the fixed illumination area, the incoming electron flux at the surface is consequently given. LEED exposure at 12.6 eV was then adjusted, the MCP switched on again and data taken within 1h to avoid a significant influence of possible drift from the FEC emission current during data acquisition.

The experimental LEED pattern was simulated using the LEEDpat software (Version 3.0).

#### Atomic force microscope

Atomic Force Microscopy was performed with an Asylum Research Cypher SPM using standard tapping mode. Tips with a nominal curvature of 7 nm, a resonance frequency of 70 kHz, and a spring constant of 2 N/m were used.

#### Scanning electron microscopy

The scanning electron microscopy images were obtained with a Zeiss Sigma VP at a beam energy of 10 kV using the in-lens detector of the system.

#### X-ray photoelectron spectroscopy

X-ray photoelectron spectroscopy was performed in a UHV Multiprobe system (Scienta Omicron) using a monochromatic X-ray source (Al K $\alpha$ ) and an electron analyzer (Argus CU) with a spectral resolution of 0.6 eV. The measurements were performed at a pressure < 2  $\times$  10<sup>-10</sup> mbar. The spectra were fitted using Voigt functions (30:70) after linear background subtraction.

#### Conflicts of interest

There are no conflicts of interest to declare.

#### Acknowledgements

We acknowledge financial support of the DFG via TRR234 "Catalight" (project no. 407463162, project B7, Z2), a research infrastructure grant INST 275/257-1 FUGG (project no. 313713174), the research grants TU149/8-2 (project no. 219397742) and WI 4691/1-1 (project no. 322051344). We acknowledge funding from the Austrian Science Fund (FWF): Y 1174-N36. We thank Stephanie Höppener and Ulrich S. Schubert for enabling the SEM characterization. The SEM facilities of the Jena Center for Soft Matter (JCSM) were established with a grant from the German Research Council (DFG). The authors thank Zian Tang for technical support.

## References

1. M. Knoll and E. Ruska, *Z. Phys.*, 1932, **79**, 699-699.
2. D. B. Williams and C. B. Carter, *The Transmission Electron Microscope*, Springer US, Boston, MA, 2019.
3. A. Mozumder and Y. Hatano, *Charged Particles and Photon Interaction with Matter: Chemical, Physicochemical, and Biological Consequences with Applications*, Marcel Dekker, New York, 2004.
4. M. Haider, S. Uhlemann, E. Schwan, H. Rose, B. Kabius and K. Urban, *Nature*, 1998, **392**, 768-769.
5. M. A. O'Keefe, C. J. D. Hetherington, Y. C. Wang, E. C. Nelson, J. H. Turner, C. Kisielowski, J. O. Malm, R. Mueller, J. Ringnald, M. Pan and A. Thust, *Ultramicroscopy*, 2001, **89**, 215-241.
6. M. Linck, P. Hartel, S. Uhlemann, F. Kahl, H. Müller, J. Zach, M. Haider, M. Niestadt, M. Bischoff, J. Biskupek, Z. Lee, T. Lehnert, F. Börrnert, H. Rose and U. Kaiser, *Phys.Rev.Lett.*, 2016, **117**, 076101.
7. M. Feldman, *Nanolithography: The Art of Fabricating Nanoelectronic and Nanophotonic Devices and Systems*, Woodhead Publishing, 2014.
8. S. T. Skowron, T. W. Chamberlain, J. Biskupek, U. Kaiser, E. Besley and A. N. Khlobystov, *Accounts Chem. Res.*, 2017, **50**, 1797-1807.
9. J. Li and F. Banhart, *Nano Letters*, 2004, **4**, 1143-1146.
10. T. W. Chamberlain, J. Biskupek, S. T. Skowron, A. V. Markevich, S. Kurasch, O. Reimer, K. E. Walker, G. A. Rance, X. Feng, K. Müllen, A. Turchanin, M. A. Lebedeva, A. G. Majouga, V. G. Nenajdenko, U. Kaiser, E. Besley and A. N. Khlobystov, *ACS Nano*, 2017, **11**, 2509-2520.
11. D. Ugarte, *Nature*, 1992, **359**, 707-709.
12. F. Banhart and P. M. Ajayan, *Nature*, 1996, **382**, 433-435.
13. W. Eck, A. Küller, M. Grunze, B. Völkel and A. Gözlhäuser, *Adv. Mater.*, 2005, **17**, 2583-2587.
14. A. Turchanin and A. Gözlhäuser, *Adv. Mater.*, 2016, **28**, 6075-6103.
15. A. Turchanin, *Chimia*, 2019, **73**, 473-479.
16. P. Angelova, H. Vieker, N.-E. Weber, D. Matei, O. Reimer, I. Meier, S. Kurasch, J. Biskupek, D. Lorbach, K. Wunderlich, L. Chen, A. Terfort, M. Klapper, K. Müllen, U. Kaiser, A. Gözlhäuser and A. Turchanin, *ACS Nano*, 2013, **7**, 6489-6497.
17. X. Zhang, C. Neumann, P. Angelova, A. Beyer and A. Gözlhäuser, *Langmuir*, 2014, **30**, 8221-8227.
18. Z. Zheng, C. T. Nottbohm, A. Turchanin, H. Muzik, A. Beyer, M. Heilemann, M. Sauer and A. Gözlhäuser, *Angew. Chem. Int. Ed.*, 2010, **49**, 8493-8497.
19. X. H. Zhang, E. Marschewski, P. Penner, A. Beyer and A. Gözlhäuser, *J. Appl. Phys.*, 2017, **122**, 7.
20. A. Turchanin, M. Schnietz, M. El-Desawy, H. H. Solak, C. David and A. Gözlhäuser, *Small*, 2007, **3**, 2114-2119.
21. X. Zhang, H. Vieker, A. Beyer and A. Gözlhäuser, *Beilstein J. Nanotech.*, 2014, **5**, 188-194.
22. A. Turchanin, D. Käfer, M. El-Desawy, C. Wöll, G. Witte and A. Gözlhäuser, *Langmuir*, 2009, **25**, 7342-7352.
23. E. Illenberger, *Chem. Rev.*, 1992, **92**, 1589-1609.
24. R. E. Palmer and P. J. Rous, *Rev. Mod. Phys.*, 1992, **64**, 383-440.
25. I. I. Fabrikant, S. Eden, N. J. Mason and J. Fedor, in *Adv. Atom. Mol. Opt. Phys.*, eds. E. Arimondo, C. C. Lin and S. F. Yelin, Academic Press, 2017, vol. 66, pp. 545-657.
26. L. Amiaud, J. Houplin, M. Bourdier, V. Humblot, R. Azria, C. M. Pradier and A. Lafosse, *PCCP*, 2014, **16**, 1050-1059.
27. J. Houplin, C. Dablemont, L. Sala, A. Lafosse and L. Amiaud, *Langmuir*, 2015, **31**, 13528-13534.
28. D. G. Matei, N.-E. Weber, S. Kurasch, S. Wundrack, M. Woszczyna, M. Grothe, T. Weimann, F. Ahlers, R. Stosch, U. Kaiser and A. Turchanin, *Adv. Mater.*, 2013, **25**, 4146-4151.
29. Y. Yang, P. Dementyev, N. Biere, D. Emmrich, P. Stohmann, R. Korzetz, X. Zhang, A. Beyer, S. Koch, D. Anselmetti and A. Gözlhäuser, *ACS Nano*, 2018, **12**, 4695-4701.
30. P. van Deursen, Z. Tang, A. Winter, M. Mohn, U. Kaiser, A. Turchanin and G. Schneider, *Nanoscale*, 2019, DOI: 10.1039/C1039NR05537A.
31. D. G. Matei, H. Muzik, A. Gözlhäuser and A. Turchanin, *Langmuir*, 2012, **28**, 13905-13911.
32. W. Eck, V. Stadler, W. Geyer, M. Zharnikov, A. Gözlhäuser and M. Grunze, *Adv. Mater.*, 2000, **12**, 805-808.
33. M. Zharnikov and M. Grunze, *J. Phys.: Condens. Matter*, 2001, **13**, 11333-11365.
34. H. Kampmann, PhD Thesis, Über das Wachstum und die Struktur Selbstorganisierender Monolagen, University Bielefeld. Bielefeld, 2014.
35. L. Kankate, A. Turchanin and A. Gözlhäuser, *Langmuir*, 2009, **25**, 10435-10438.
36. J. C. Love, L. A. Estroff, J. K. Kriebel, R. G. Nuzzo and G. M. Whitesides, *Chem. Rev.*, 2005, **105**, 1103-1170.
37. C. Olsen and P. A. Rowntree, *J. Chem. Phys.*, 1998, **108**, 3750-3764.
38. Y.-K. Kim, K. K. Irikura, M. E. Rudd, M. A. Ali, P. M. Stone, J. Chang, J. S. Coursey, R. A. Dragoset, A. R. Kishore, K. J. Olsen, A. M. Sansonetti, G. G. Wiersma, D. S. Zucker and M. A. Zucker, *NIST Standard Reference Database 107*, 2004.
39. W. Hwang, Y. K. Kim and M. E. Rudd, *J. Chem. Phys.*, 1996, **104**, 2956-2966.
40. B. Völkel, A. Gözlhäuser, H. U. Müller, C. David and M. Grunze, *J. Vac. Sci. Technol. B*, 1997, **15**, 2877-2881.
41. L. A. Gonzalez, M. Angelucci, R. Larciprete and R. Cimino, *AIP Adv.*, 2017, **7**, 115203.
42. M. Woszczyna, A. Winter, M. Grothe, A. Willunat, S. Wundrack, R. Stosch, T. Weimann, F. Ahlers and A. Turchanin, *Adv. Mater.*, 2014, **26**, 4831-4837.
43. A. Winter, Y. Ekinci, A. Gözlhäuser and A. Turchanin, *2D Mater.*, 2019, **6**, 021002.

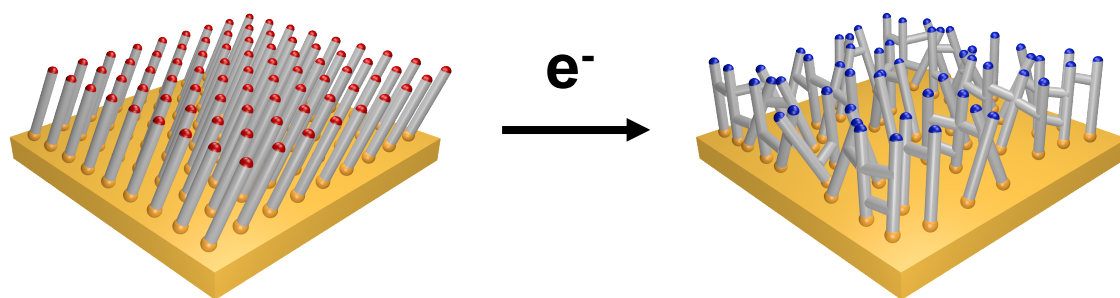


**Figure 1:** Schematic representation of the crosslinking process. The initially ordered NBPT SAM is converted into a CNM using low-energy electrons (2.5 – 100 eV) by the formation of new intermolecular bonds. Additionally, the nitrogroup (red) is reduced to an amino group (blue).

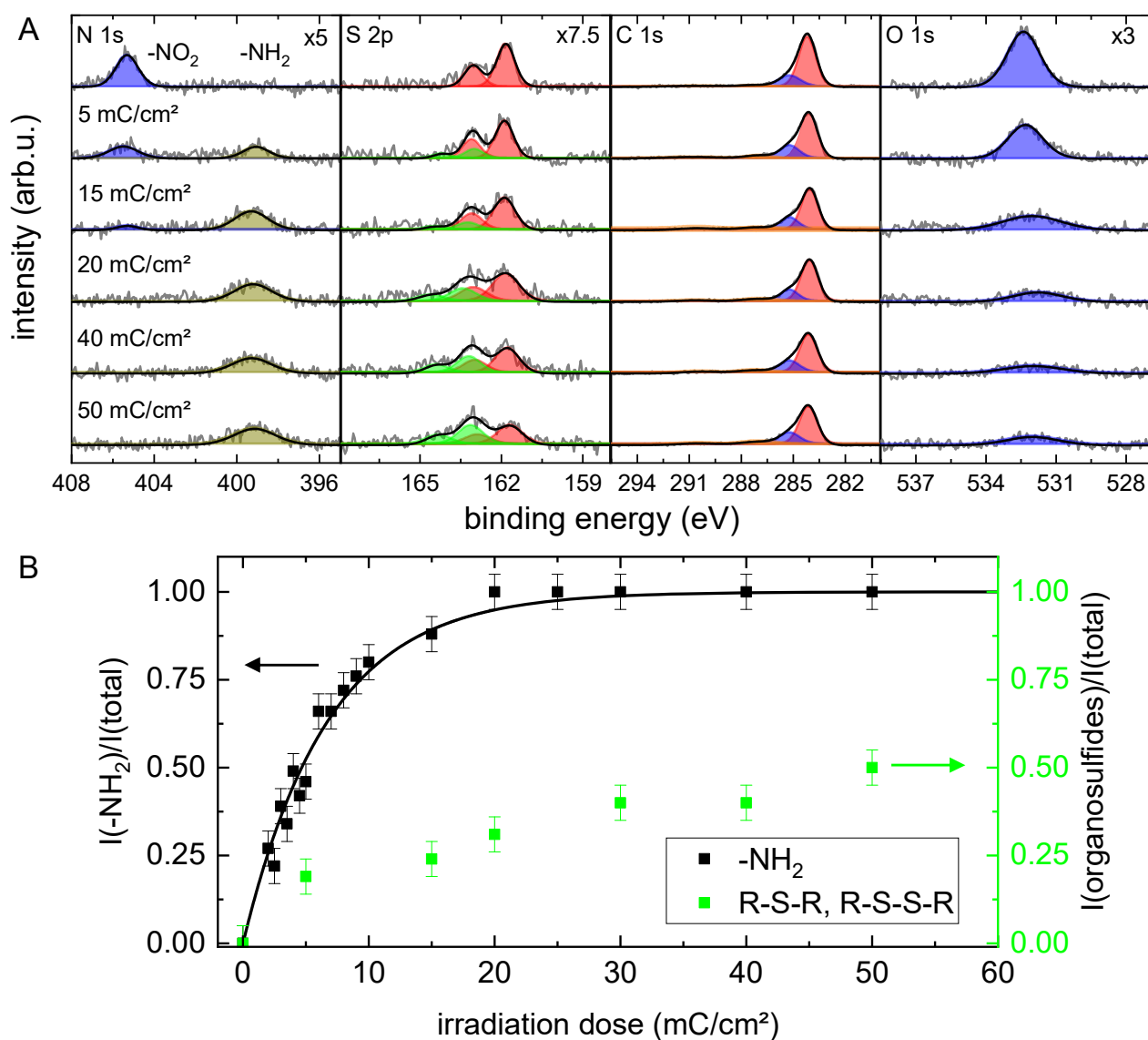


**Figure 2:** (A) N 1s, S 2p, C 1s and O 1s XPS spectra of a NBPT SAM which is stepwise irradiated with electrons with an energy of 50 eV and subsequently crosslinked into a Carbon Nanomembrane. For better representation, intensities of the N 1s, S 2p and O 1s spectra are multiplied by the factor presented in the figure. (B) fraction of -NH<sub>2</sub> and organosulfide (R-S-R and R-S-S-R) groups, respectively, for different irradiation doses determined by the XPS results presented in (A)

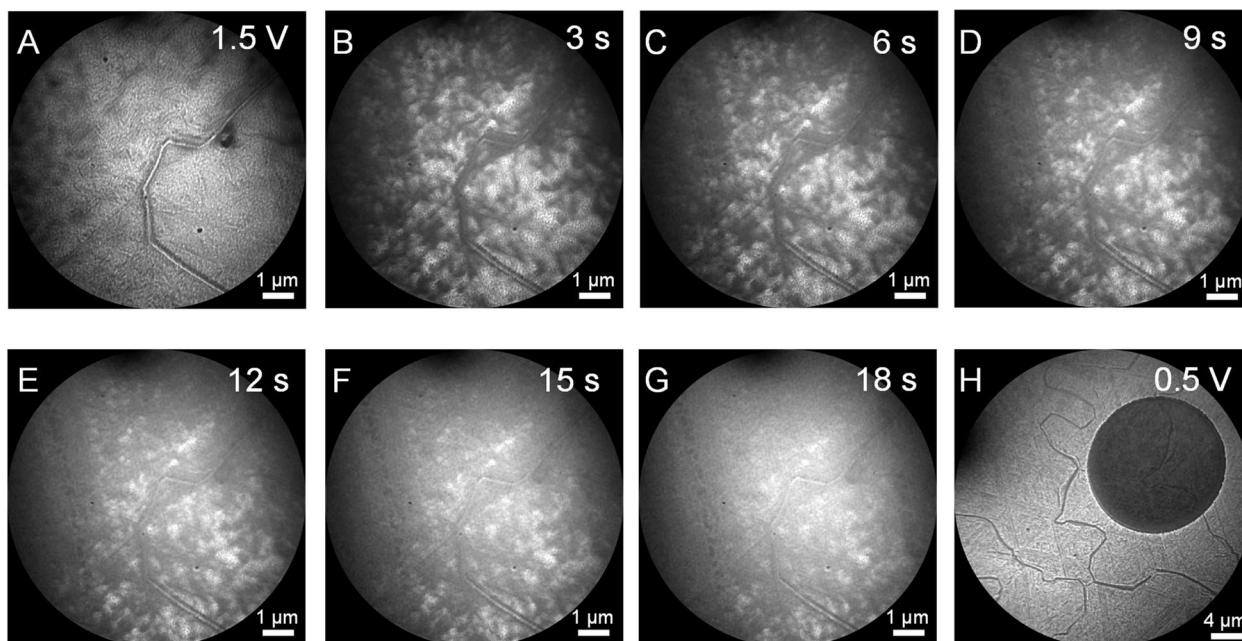


**Figure 3:** A-G series of LEEM images obtained on an NBPT SAM on Au/mica using 1.5 V electron energy. The sample was illuminated stepwise for 3 seconds between each image using 50 V electron energy. The darker phase according to crosslinked areas is growing especially between A and B. The different contrast is especially visible in a bigger field of view (H). The LEEM images A –G were obtained using a contrast aperture, the image H was acquired without contrast aperture.

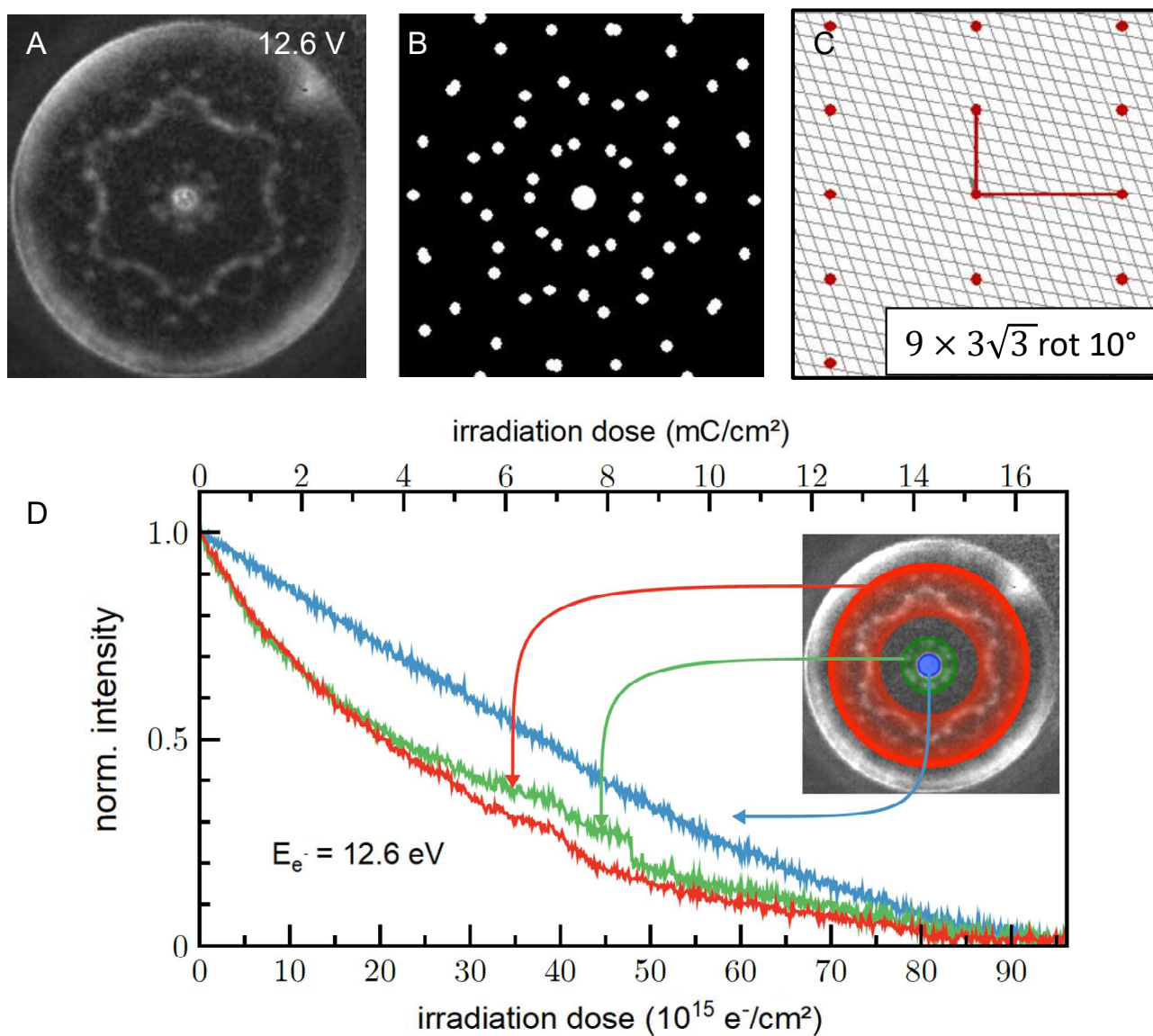


**Figure 4:** (A)  $\mu$ LEED pattern of an NBPT SAM, (B) simulated pattern (C) Schematic drawings of the unit cell used for the simulation of the LEED pattern (D) Intensity of the  $\mu$ LEED spots in dependence of the irradiation dose.

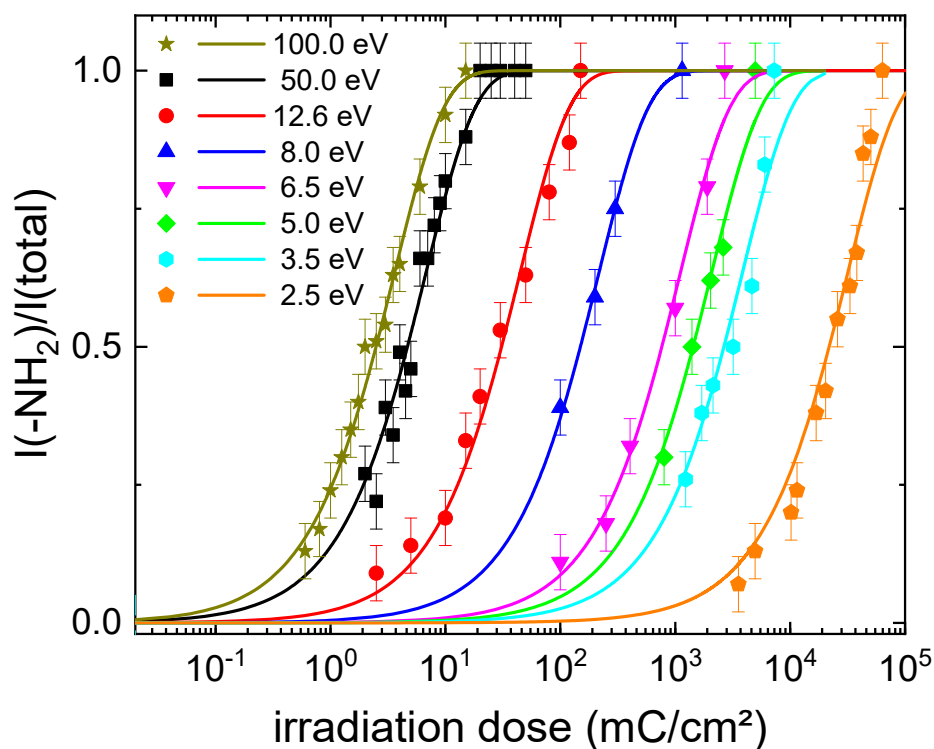


**Figure 5:** Summary of the low-energy electron irradiation using different electron energies between 2.5 eV and 100 eV. The conversion into CNMs estimated by the fraction of amino groups determined by the XPS data shows the high energy dependency of the crosslinking process.

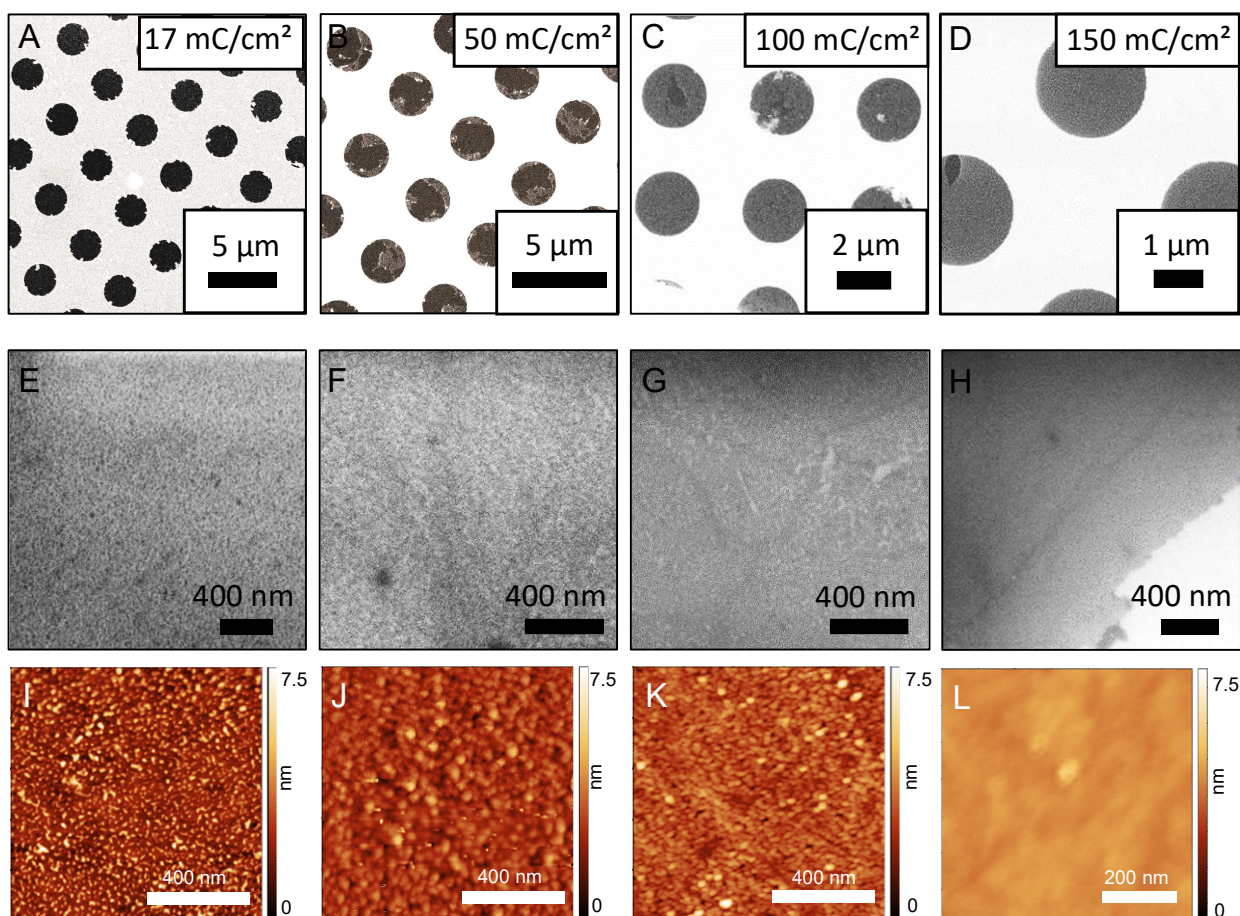


**Figure 6:** (A-D) Scanning electron microscope (SEM) images of NBPT samples irradiated with different doses using an electron energy of 12.6 eV and transferred onto TEM grids. For a complete crosslinking an electron dose of 150 mC/cm<sup>2</sup> is required. (E-H) SEM and (I-L) AFM images after transfer onto SiO<sub>2</sub>/Si wafer show the transfer of individual crosslinked patches. After an electron dose of 150 mC/cm<sup>2</sup> the patches are linked together leading to a smooth molecular nanosheet.

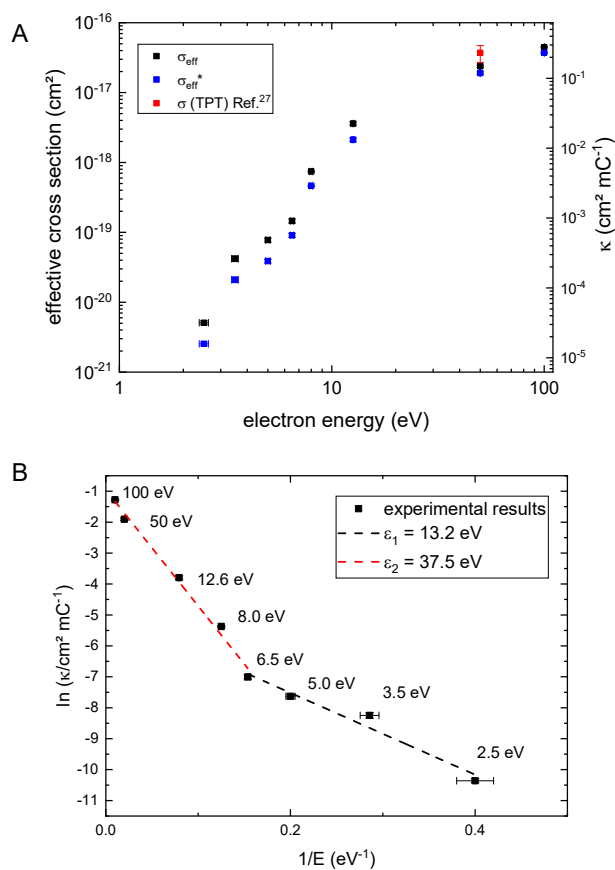


**Figure 7:** (A) Presentation of experimentally obtained coefficients  $\kappa$  from the function  $F(\Phi)$  for the different electron energies. This value was used to calculate the effective cross section,  $\sigma_{\text{eff}}$ , and the secondary electron corrected  $\sigma_{\text{eff}}^*$ . The published  $\sigma$  for TPT irradiated with an electron energy of 50 eV is added in the graph. (B) Arrhenius like plot of the data presented in (A). The results follow both a linear trend for energies of 2.5 – 6.5 eV and 6.5 – 100 eV.

## Supporting Information

### **Low-energy electron irradiation induced synthesis of molecular nanosheets: An influence of the electron beam energy**

Christof Neumann,<sup>a</sup> Richard A. Wilhelm,<sup>bc</sup> Maria Küllmer,<sup>a</sup> and Andrey Turchanin<sup>ad\*</sup>

<sup>a</sup> *Institute of Physical Chemistry, Friedrich Schiller University Jena, 07743 Jena, Germany*

<sup>b</sup> *Institute of Applied Physics, TU Wien, 1040 Vienna, Austria*

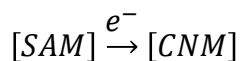
<sup>c</sup> *Institute of Ion Beam Physics and Materials Research, Helmholtz-Zentrum Dresden-Rossendorf, 01328 Dresden, Germany*

<sup>d</sup> *Jena Center for Soft Matter (JCSM), 07743 Jena, Germany*

\*Address correspondence to [andrey.turchanin@uni-jena.de](mailto:andrey.turchanin@uni-jena.de)

### Derivation of the rate equation for conversion of a NBPT SAM into a CNM

We described the crosslinking of the SAM into a CNM using electron induced crosslinking with the following chemical equation:



Here, [SAM] and [CNM] represent the fraction of the nitro groups and amino groups in the monolayer, respectively. We assume the reaction can be expressed by a first-order rate equation with the rate constant,  $\kappa$ , and the electron dose,  $\phi$ :

$$\begin{aligned} \frac{d[SAM]}{d\phi} &= -\kappa[SAM] \\ \Leftrightarrow \frac{d[SAM]}{[SAM]} &= -\kappa d\phi \\ \Rightarrow \int_{[SAM]_0}^{[SAM]} \frac{d[SAM]}{[SAM]} &= \int_0^\phi -\kappa d\phi \\ \Leftrightarrow \ln([SAM]) \Big|_{[SAM]_0}^{[SAM]} &= -\kappa\phi \Big|_0^\phi \\ \Leftrightarrow \ln([SAM]) - \ln([SAM]_0) &= -\kappa\phi \end{aligned}$$

Initially, the sample consist completely of a SAM and we can simplify using  $[SAM]_0 = 1$ :

$$\begin{aligned} \ln([SAM]) &= -\kappa\phi \\ [SAM] &= e^{-\kappa\phi} \end{aligned}$$

We conclude from our XPS results  $[SAM] + [CNM] = 1$  leading to:

$$F(\phi) = [CNM](\phi) = 1 - e^{-\kappa\phi}$$

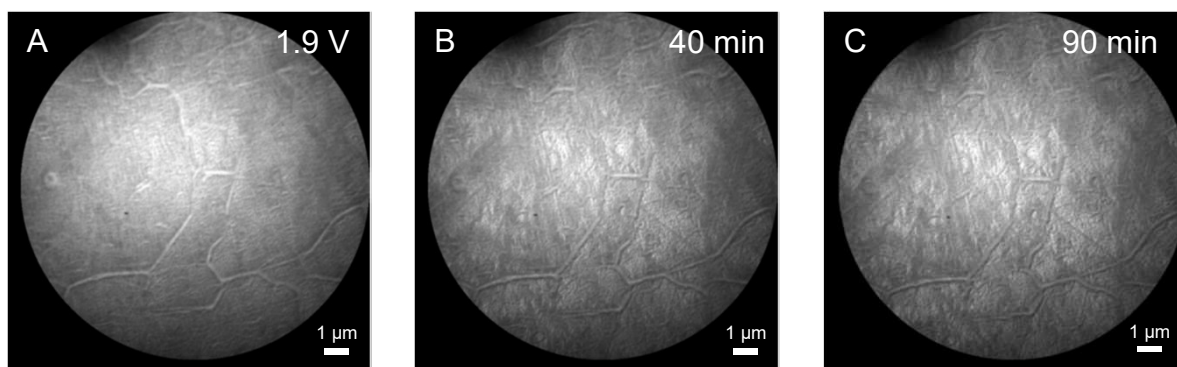


**Figure S1:** LEEM images acquired by continuous illumination of the NBPT SAM using an electron energy of 1.9 eV. Image A shows the pristine SAM, whereby the images B and C are acquired after 40 min and 90 min, respectively.

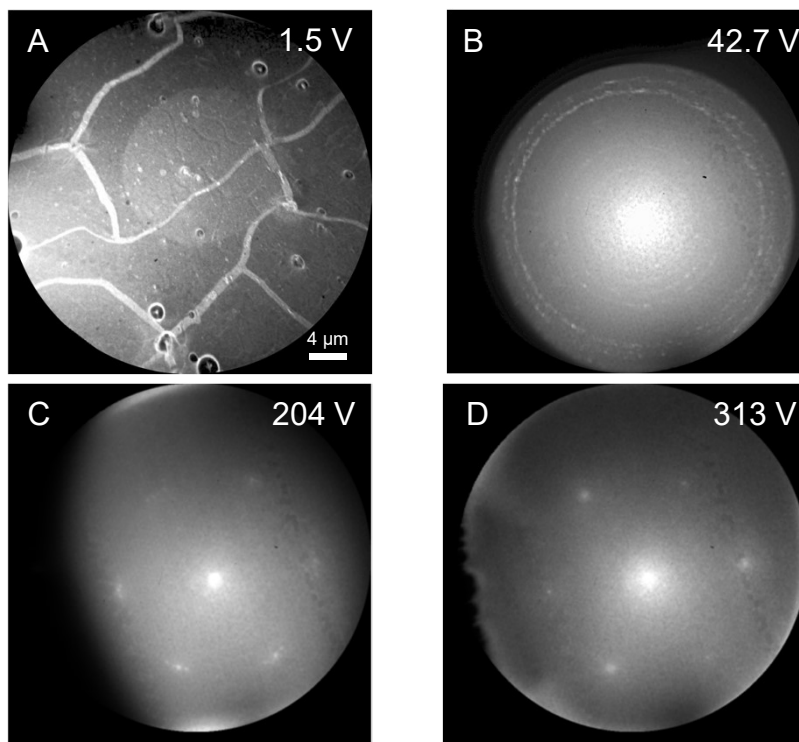


**Figure S2:** (A) LEEM image of the Au/mica sample showing different domains. The images was obtained without contrast aperture. (B)  $\mu$ LEED pattern acquired on an Au/mica reference sample using an electron energy of 42.7 eV. The  $\mu$ LEED pattern was acquired within the circular region in the center of (A) (C-D)  $\mu$ LEED pattern acquired on an NBPT SAM/Au/mica using higher electron energies showing the pattern of a Au(111) domain.

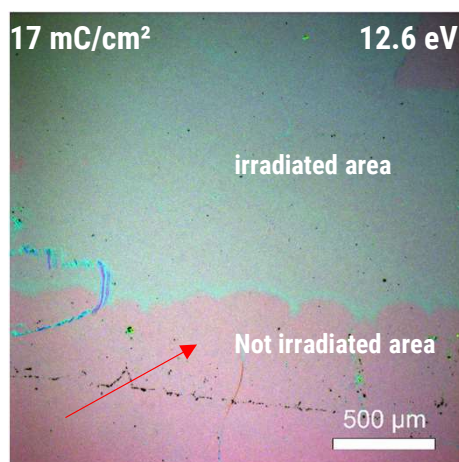


**Figure S3:** Optical microscope image of a transferred NBPT CNM after irradiation with 17 mC/cm<sup>2</sup> using an electron energy of 12.6 eV. The area marked with the red arrow was covered during electron irradiation by the sample holder.

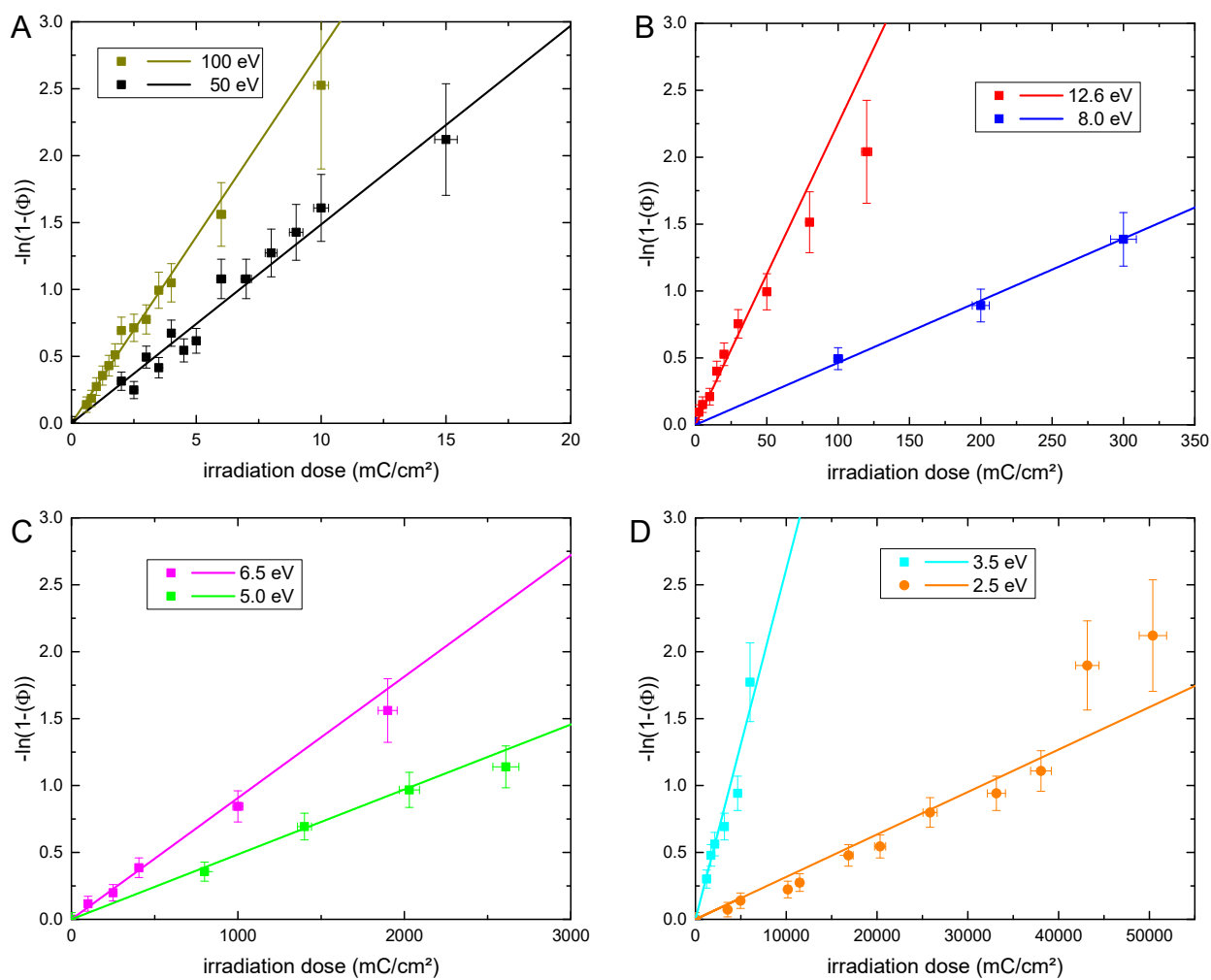


**Figure S4:** Experimental data presented in Fig. 5A and the linearized fit function  $F(\phi)$ . For better visualization the curves are presented in different irradiation dose regimes (A-D). The linearized fit functions show a good agreement with the experimental data.

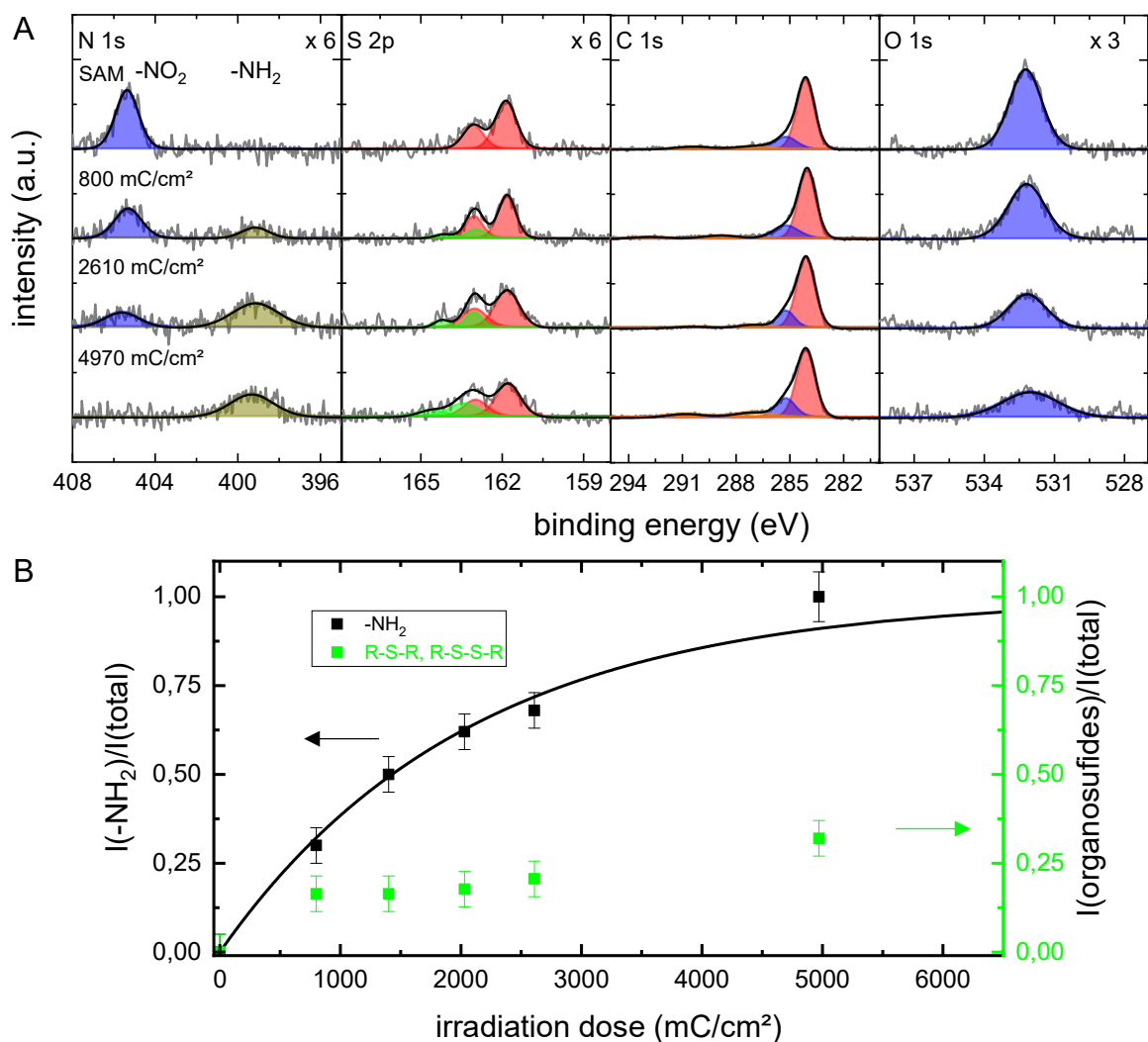


**Figure S5** : (A) N 1s, S 2p, C 1s and O 1s XP spectra of a NBPT SAM which is stepwise irradiated with electrons with an energy of 5 eV and subsequently cross-linked into a Carbon Nanomembrane. For better representation, intensities of the N 1s, S 2p and O 1s spectra are multiplied by the factor presented in the figure. (B) fraction of  $-\text{NH}_2$  and organosulfide (R-S-R and R-S-S-R) groups, respectively, for different irradiation doses determined by the XPS results presented in (A)

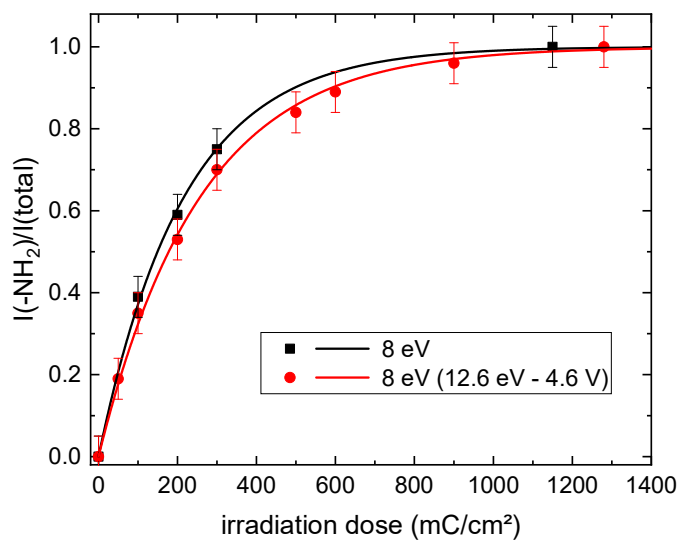


**Figure S5:** XPS analysis of the cross-linking of an NBPT SAM using 8 eV electron energy and 12.6 eV, whereby the sample was biased with 4.6 V. The resulting fraction of amino groups is identical for both samples in dependence of the irradiation dose.

**Table S1:** Coefficient of determination,  $R^2$ , of the linearized fit function  $F(\phi)$  in Fig S4.

Electron energy (eV)	100.0	50.0	12.6	8.0	6.5	5.0	3.5	2.5
$R^2$	0.992	0.976	0.984	0.999	0.988	0.983	0.946	0.958

**Table S2:** Summary of the determined rate constants  $\kappa$ . These values were used to calculate the effective cross-linking cross section  $\sigma_{\text{eff}}$  and the cross section  $\sigma_{\text{eff}}^*$ , corrected by the contribution of the secondary electrons.

<b>E (eV)</b>	<b><math>\kappa</math> (cm<sup>2</sup>/mC)</b>	<b><math>\sigma</math> (cm<sup>2</sup>)</b>	<b><math>\sigma^*</math> (cm<sup>2</sup>)</b>
100.0	$(2.79 \pm 0.07) \times 10^{-1}$	$(4.47 \pm 0.11) \times 10^{-17}$	$(3.72 \pm 0.09) \times 10^{-17}$
50.0	$(1.49 \pm 0.06) \times 10^{-1}$	$(2.38 \pm 0.09) \times 10^{-17}$	$(1.90 \pm 0.08) \times 10^{-17}$
12.6	$(2.25 \pm 0.13) \times 10^{-2}$	$(3.61 \pm 0.20) \times 10^{-18}$	$(2.12 \pm 0.12) \times 10^{-18}$
8.0	$(4.64 \pm 0.10) \times 10^{-3}$	$(7.43 \pm 0.16) \times 10^{-19}$	$(4.64 \pm 0.10) \times 10^{-19}$
6.5	$(9.07 \pm 0.61) \times 10^{-4}$	$(1.45 \pm 0.10) \times 10^{-19}$	$(9.08 \pm 0.61) \times 10^{-20}$
5.0	$(4.85 \pm 0.31) \times 10^{-4}$	$(7.77 \pm 0.49) \times 10^{-20}$	$(3.89 \pm 0.25) \times 10^{-20}$
3.5	$(2.62 \pm 0.23) \times 10^{-4}$	$(4.19 \pm 0.37) \times 10^{-20}$	$(2.10 \pm 0.19) \times 10^{-20}$
2.5	$(3.17 \pm 0.21) \times 10^{-5}$	$(5.08 \pm 0.33) \times 10^{-21}$	$(2.54 \pm 0.17) \times 10^{-21}$

**Table S3:** Secondary electron yield (SEY) for primary electrons,  $n_p$ , with different energies adopted from Refs. [1-2]. For 50-100 eV only elastically scattered electrons are taken into account. The number of electrons,  $N$ , involved in the cross-linking process is calculated to  $N = n_p(1 + \eta_{SEY})$

<b>Electron energy (eV)</b>	<b>100.0</b>	<b>50.0</b>	<b>12.6</b>	<b>8.0</b>	<b>6.5</b>	<b>5.0</b>	<b>3.5</b>	<b>2.5</b>
$\eta_{SEY}$	0.2	0.25	0.7	0.6	0.6	1.0	1.0	1.0

[1] B. Völkel, A. Götzhäuser, H. U. Müller, C. David and M. Grunze, *J. Vac. Sci. Tech. B.*, 1997, **15**, 2877-2881.

[2] L. A. Gonzalez, M. Angelucci, R. Larciprete and R. Cimino, *AIP Adv.*, 2017, **7**, 115203.

**Video S1:** Video of the *in operando* 12.6 eV  $\mu$ LEED diffraction pattern as a function of the applied the irradiation dose.